

Synaptic vesicle proteins and ATG9A self-organize in distinct vesicle phases within synapsin condensates

Received: 17 July 2022

Accepted: 16 January 2023

Published online: 28 January 2023

 Check for updatesDaehun Park^{1,2,3,4}, Yumei Wu^{1,2,3,4}, Xinbo Wang^{1,2,3,4},
Swetha Gowrishankar⁵, Aaron Baublis⁶ & Pietro De Camilli^{1,2,3,4,7} ✉

Ectopic expression in fibroblasts of synapsin 1 and synaptophysin is sufficient to generate condensates of vesicles highly reminiscent of synaptic vesicle (SV) clusters and with liquid-like properties. Here we show that unlike synaptophysin, other major integral SV membrane proteins fail to form condensates with synapsin, but co-assemble into the clusters formed by synaptophysin and synapsin in this ectopic expression system. Another vesicle membrane protein, ATG9A, undergoes activity-dependent exocytosis at synapses, raising questions about the relation of ATG9A traffic to the traffic of SVs. We find that both in fibroblasts and in nerve terminals ATG9A does not co-assemble into synaptophysin-positive vesicle condensates but localizes on a distinct class of vesicles that also assembles with synapsin but into a distinct phase. Our findings suggest that ATG9A undergoes differential sorting relative to SV proteins and also point to a dual role of synapsin in controlling clustering at synapses of SVs and ATG9A vesicles.

A defining characteristic of presynaptic sites in the nervous system is the presence of clusters of neurotransmitter containing synaptic vesicles (SVs) anchored to the presynaptic plasma membrane¹. Upon nerve terminal depolarization, SVs close to the plasma membrane undergo exocytosis to release their neurotransmitter content². Their membranes are then rapidly recaptured by endocytosis and reused for the generation of new SVs that re-enter the vesicle cluster^{3–6}. Recent studies have implicated liquid-liquid phase separation as an organizing principle in the assembly of these clusters and have pointed to the protein synapsin as to a key player in these assemblies, also referred henceforth as condensates^{7–9}. Synapsin, a dimeric protein associated with SVs by low-affinity charge-based interactions, has the intrinsic property to phase separate and captures SVs into its phase^{9–11}. Loss of synapsin

function by genetic perturbation or by antibody injection results in the dispersion of SVs with the exception of those directly tethered the “active zones” of secretion^{9,12–14}. Conversely, synapsin can induce vesicle clusters when expressed together with the major SV protein synaptophysin in fibroblasts¹⁵, cells which physiologically do not express either protein. When expressed alone in this exogenous system, synaptophysin is targeted to small sparse vesicles that can be labeled by endocytic tracers^{16,17}. Upon coexpression with synapsin these vesicles become assembled in large clusters that are morphologically very similar to those found in presynaptic nerve terminals and that share with these clusters liquid properties¹⁵. Interestingly, several other SV proteins tested do not induce the formation of SV-like clusters when co-expressed with synapsin¹⁵. These results open the possibility of

¹Department of Neuroscience, Yale University School of Medicine, New Haven, CT 06510, USA. ²Department of Cell Biology, Yale University School of Medicine, New Haven, CT 06510, USA. ³Howard Hughes Medical Institute, Yale University School of Medicine, New Haven, CT 06510, USA. ⁴Program in Cellular Neuroscience, Neurodegeneration, and Repair, Yale University School of Medicine, New Haven, CT 06510, USA. ⁵Department of Anatomy and Cell Biology, College of Medicine, University of Illinois at Chicago, Chicago, IL 60612, USA. ⁶Harvard Chan Advanced Multi-omics Platform, Harvard T.H. Chan School of Public Health, Boston, MA 02115, USA. ⁷Kavli Institute for Neuroscience, Yale University School of Medicine, New Haven, CT 06510, USA.

✉ e-mail: pietro.decamilli@yale.edu

exploiting this experimental model to gain further insight into SV biogenesis and into the traffic of SV proteins relative to other proteins.

An open question in the cell biology of the presynapse is the relation between the traffic of SV proteins and the traffic of ATG9A. ATG9A is a lipid scramblase^{18–20} required for the growth and expansion of the autophagic membrane and the only transmembrane protein of the core autophagy machinery^{21,22}. ATG9A is present in axon terminals where, together with other autophagy factors, it plays an important role in synapse development and homeostasis^{23–25}. Proteomic studies have detected ATG9A (at low copy number) in purified SV fractions^{26–28}. Moreover, recent imaging studies have shown that synaptically localized ATG9A undergoes exo-endocytosis in response to activity in parallel with bona fide SV proteins^{23,25}. However, how traffic of ATG9A vesicles in nerve terminals relates to that of SVs remains elusive.

Here, we have used the vesicle cluster reconstitution system in non-neuronal cells to gain insight into the traffic of ATG9A relative to the traffic of SV proteins. More specifically, we investigated which exogenous proteins can be recruited to the synaptophysin and synapsin-positive vesicle condensates. We have found that all of several bona fide SV proteins tested (VAMP2, SCAMP5, synaptotagmin 1, vGlut1, vGAT1, Rab3A) accumulate into the vesicle condensates in COS7 cells formed by synaptophysin and synapsin. However, we also found that ATG9A does not assemble into them. ATG9A is a component of a distinct set of slightly larger vesicles that can also be clustered by synapsin. Moreover, when both synaptophysin and ATG9A are co-expressed with synapsin, synaptophysin vesicles and ATG9A vesicles segregate in different subphases within the synapsin phase. Proteomic analysis further showed a clear distinct composition of the synaptophysin and ATG9A vesicles in this experimental model. A segregation of synaptophysin from ATG9A within nerve terminals was also observed when fluorescently tagged ATG9A and synaptophysin-HA were expressed in neurons or when the endogenous proteins were detected with antibodies. Collectively, our studies suggest a differential sorting of SV proteins and ATG9A in axon endings and the property of synapsin to capture both bona fide SVs and ATG9A vesicles in proximity of presynaptic sites.

Results

Synaptophysin and synapsin clusters in fibroblasts recruit other SV components

As we described previously¹⁵, coexpression of synaptophysin (Synp) and mCherry-synapsin 1a (mCherry-Syn) in COS7 cells results in the formation of clusters of small vesicles that are similar in size to SVs (Fig. 1a, b). Moreover, like bona fide SVs, the small vesicles can be labeled by the extracellular tracer cholera toxin-horseradish peroxidase (CTX-HRP), revealing an endocytic origin¹⁵ (Fig. 1b). These vesicle clusters (also referred to as vesicle condensates), appear as large droplets sparse throughout the cytoplasm in fluorescence microscopy (Fig. 1a). Co-expression with synapsin of several other SV proteins²⁹ such as secretory carrier membrane 5 (EGFP-SCAMP5), the vesicular glutamate transporter (vGlut fuse to pHluorin, vGlut-pH) and synaptotagmin 1 (SYT1-EGFP) did not result in the formation of similar clusters¹⁵ (Fig. 1a). SCAMP5 and vGlut localized to sparse vesicles and SYT1 had a predominant plasma membrane localization, as demonstrated in several previous studies^{15,30} (Fig. 1a). We confirmed these studies and additionally tested other SV proteins²⁹: vesicle-associated membrane 2 (VAMP2-pHluorin, VAMP2-pH), the vesicular GABA transporter (vGAT-pHluorin, vGAT-pH) and Rab3A (EGFP-Rab3A). We found that none of them formed condensates with synapsin, which had a diffuse cytosolic distribution irrespective of the co-expression of these proteins (Fig. 1a). The transferrin receptor (transferrin-pHluorin, TfR-pH), a protein that undergoes exo-endocytic recycling and that was previously shown to colocalize with synaptophysin when this is expressed in fibroblasts¹⁶, also did not form condensates with synapsin (Fig. 1a).

However, when these other SV proteins were expressed in COS7 cells together with synaptophysin and with synapsin, all of them co-assembled into the synaptophysin/synapsin condensates (Fig. 1c and Supplementary Fig. 1a–c). Thus, synaptophysin (1) helps nucleate vesicles into which other SV proteins are sorted and (2) drives assembly of these vesicles into condensates via its low affinity, primarily charge-based interaction, with synapsin¹⁵. Synaptophysin vesicles may represent the expansion of a physiologically occurring endocytic vesicular compartment, as they are also positive for the transferrin receptor and have an acidic lumen—a feature of house-keeping endocytic vesicles—as shown by alkalization with NH₄Cl of cells expressing VAMP2-pH (Supplementary Fig. 1d, e).

The liquid nature of vesicle clusters in fibroblasts mimics a property of SV clusters in nerve terminals

We previously showed that condensates of synapsin and synaptophysin have liquid-like property¹⁵. A similar characteristic of the clusters of synaptophysin, other SV membrane proteins and synapsin was demonstrated by their property to coalesce with each other and to undergo fluorescence recovery after photobleaching, as exemplified by droplets comprising EGFP-SCAMP5, mCherry-synapsin and synaptophysin (Fig. 2a–d). Not surprisingly, recovery of mCherry-synapsin, a peripheral membrane protein, is much faster than the recovery of an integral vesicle protein, EGFP-SCAMP5, which reflects vesicle exchange between droplets (Fig. 2b–d). A similar very fast recovery after photobleaching was observed for mCherry-synapsin in condensates present in nerve terminals (Supplementary Fig. 2a, b). Further supporting the role of phase separation mechanisms mediated by synapsin in the formation of the condensates, the droplets containing VAMP2-pH, synaptophysin and mCherry-synapsin were reversibly dissolved by 1,6-Hexanediol (1,6-HD) (Fig. 2e and Supplementary Video 1).

Our hypothesis that vesicle clusters in fibroblasts represent a model of bona fide SV clusters at synapses implies that bona fide SVs in nerve terminals must exhibit the same striking response to 1,6-Hexanediol. This was never tested so far, although the liquid nature of SV clusters was inferred indirectly from the many known properties of such clusters⁷. To address this question, we cultured mouse hippocampal neurons expressing EGFP-SCAMP5 and mCherry-synapsin. Under resting conditions, the fluorescence of the two proteins had the typical (and identical) punctate localization in peripheral axonal branches that reflects presynaptic SV clusters³¹ (Fig. 2f). Similar to what we had observed in fibroblasts (Fig. 2e and Supplementary Video 1), these puncta rapidly (within 1 min) dispersed after addition of 1,6-Hexanediol (Fig. 2f–h and Supplementary Video 2), indicating spreading of SVs along the axon. After washout, they rapidly reassembled at sites of pre-existing clusters (Fig. 2f, i). 1,4-Butanediol (1,4-BD), an alcohol with lower hydrophobicity^{32,33}, was much less effective in dispersing mCherry-synapsin condensates in cultured neurons consistent with our previous finding in fibroblasts¹⁵ (Supplementary Fig. 2c–e). The conclusion that the 1,6-Hexanediol dependent dispersion of the EGFP-SCAMP5 and mCherry-synapsin fluorescence in nerve terminals reflected the dispersion of SVs was confirmed by electron microscopy (Fig. 2j and Supplementary Fig. 3).

The dispersed and clustered state of SVs correlated with a strong difference in exocytosis in response to depolarization. The secretory response, as assessed by vGlut-pHluorin fluorescence in neurons expressing vGlut-pHluorin (and mCherry-synapsin), was much higher when SVs were clustered at presynaptic sites than during exposure to 1,6-Hexanediol, when they were dispersed (Fig. 2k, l and Supplementary Fig. 4; Supplementary Video 3).

Condensates of ATG9A-positive vesicles upon co-expression of ATG9A with synapsin

We next investigated the relation of ATG9A to SVs. As previously described^{34,35}, when expressed alone, ATG9A-EGFP was enriched in the

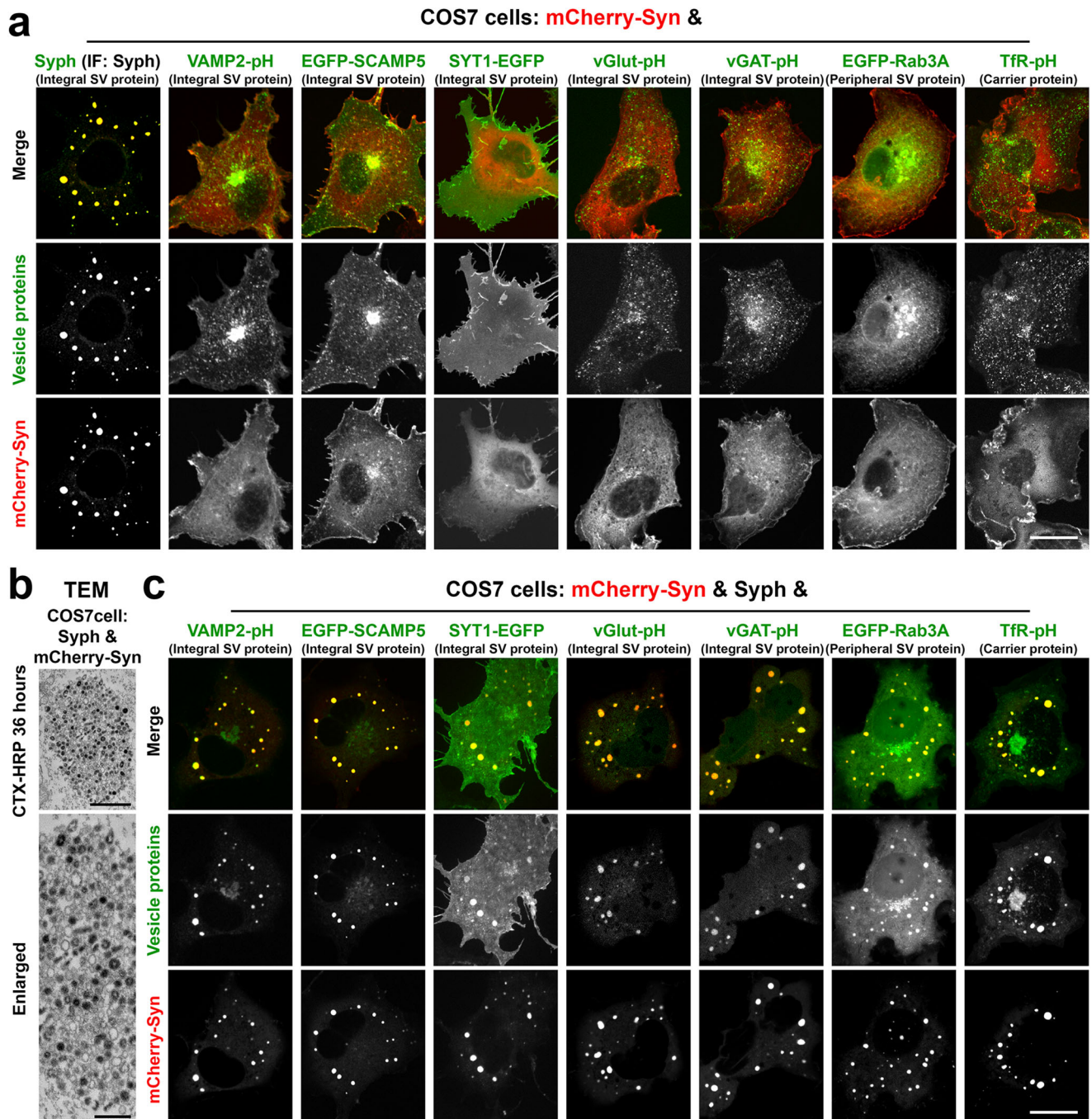
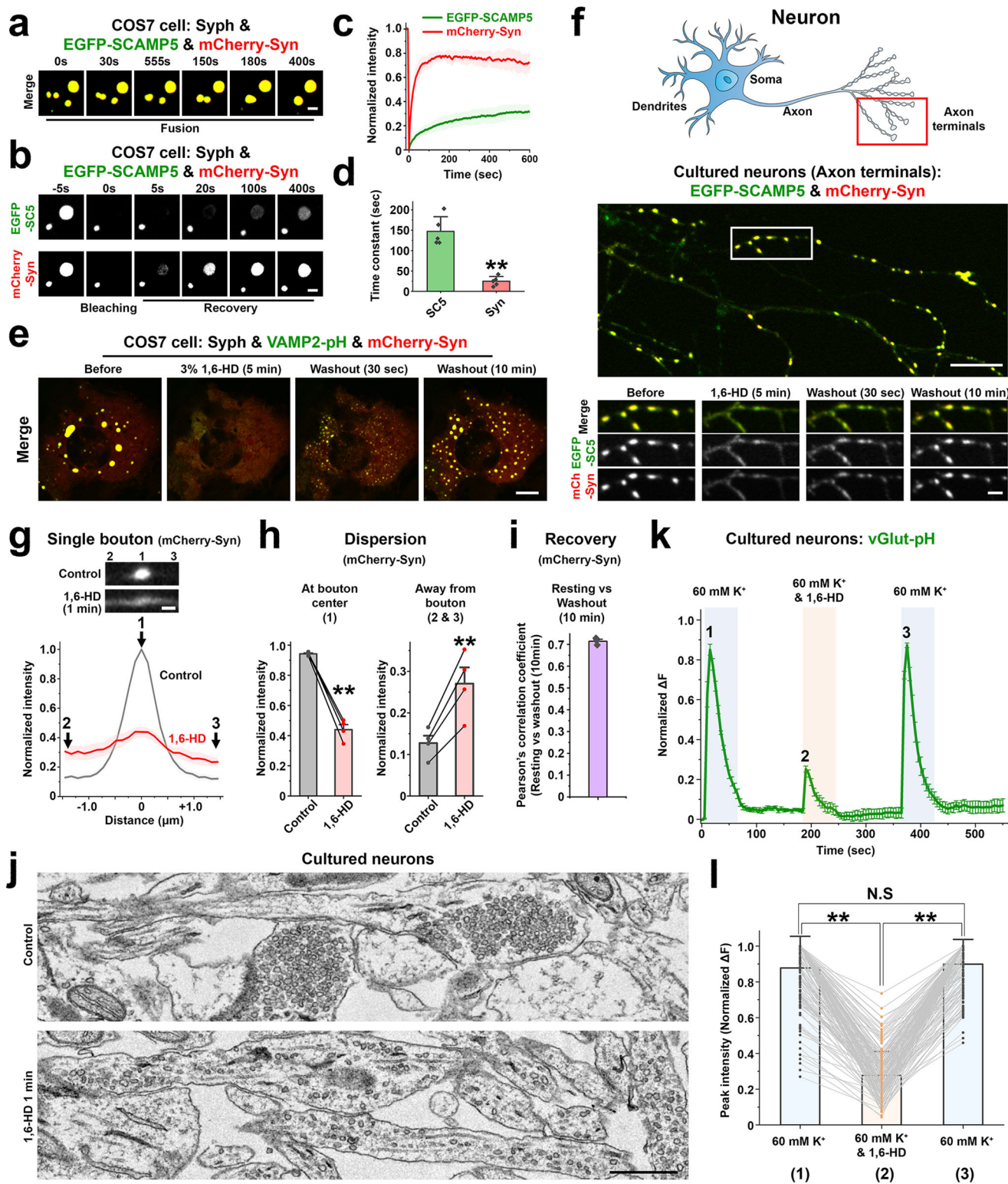


Fig. 1 | Synaptophysin and synapsin condensates recruit other SV proteins.
a COS7 cells were co-transfected with mCherry-synapsin 1a (Syn) and one of these proteins as indicated: synaptophysin (Syph) (untagged), VAMP2-pHluorin (VAMP2-pH), EGFP-SCAMP5, synaptotagmin 1-EGFP (SYT1-EGFP), vesicular glutamate transporter 1-pHluorin (vGlut-pH), vesicular GABA transporter-pHluorin (vGAT-pH), EGFP-Rab3A, and transferrin receptor-pHluorin (TfR-pH). Synaptophysin, which was untagged, was revealed by immunofluorescence. Only cells that co-express mCherry-synapsin and synaptophysin show large droplets.
b Synaptophysin and mCherry-synapsin expressing COS7 cells were exposed to

10 μ g/ml cholera toxin conjugated HRP (CTX-HRP) for 36 h, then fixed, processed for HRP reactivity and embedded for transmission electron microscopy (TEM). Black vesicles are the vesicles labeled by the endocytic tracer CTX-HRP. **c** COS7 cells were triple transfected with synaptophysin, mCherry-synapsin and one other fluorescent fusion protein as in field a. Note that all SV proteins and the transferrin receptor co-assemble into the droplets formed by synaptophysin and mCherry-synapsin. See also Supplementary Fig. 1. Scale bars, **a** = 20 μ m, **b** = 500 nm (top) and 200 nm (bottom), **c** = 20 μ m.

Golgi complex, but also localized in scattered puncta throughout the cytoplasm (Fig. 3a). Surprisingly, when co-expressed together with mCherry-synapsin, ATG9A formed large droplets (Fig. 3b) similar to those found in synaptophysin and mCherry-synapsin expressing cells (Fig. 1a). Large droplets were also observed when ATG9A was expressed with other synapsin isoforms, synapsin 2a or 3a (Supplementary Fig. 5). Correlative light-electron microscopy (CLEM) further revealed

that ATG9A-EGFP and mCherry-synapsin droplets represented clusters of small vesicles (Fig. 3c) that resemble the synaptophysin and mCherry-synapsin condensates (Fig. 1b), although the ATG9A vesicles were slightly larger [diameter: 41.8 nm (synaptophysin) vs. 54.9 nm (ATG9A)] (Fig. 3d). As in the case of synaptophysin vesicles, the vesicles in ATG9A-EGFP and mCherry-synapsin condensates could be labeled by the endocytic tracer CTX-HRP (Fig. 3e), indicating that they



are part of the endocytic system. Moreover, CTX-HRP labeled ATG9A-EGFP vesicles intermixed at random with unlabeled vesicles consistent with a liquid-like nature of the vesicle clusters (Fig. 3e). Thus, similarly to synaptophysin, but in contrast to other SV proteins tested, ATG9A, when expressed in fibroblasts without synaptophysin accumulated in vesicles that could be trapped into liquid condensates by an interaction with synapsin.

We had shown that a feature of synaptophysin that was at least in part responsible for its property to co-assemble with synapsin was its

negatively charged cytoplasmic tail, which establishes charge-based interactions with the highly positively charged C-terminal region of synapsin¹⁵. As ATG9A also has a negatively charged cytosolic tail, which could establish electrostatic interactions with synapsin (Fig. 3f), we performed the same in vitro assay based on purified recombinant proteins that we had used to analyze the interaction of synaptophysin with synapsin¹⁵. When purified synapsin and the purified cytosolic C-terminal region of ATG9A (ATG9A Ct) (Fig. 3g) were incubated in a buffer with a salt concentration in the physiological

Fig. 2 | Liquid-like properties of vesicle clusters in fibroblasts and of SV clusters in cultured neurons. a–e COS7 cells were transfected as indicated. **a**, Fusion of droplets. **b–d** Fluorescence recovery of EGFP-SCAMP5 and mCherry-synapsin after photobleaching of a single droplet. Data are represented as mean \pm SD ($n = 5$ droplets). $**p < 0.01$, by two-sided Student's *t*-test. **e** Droplets comprising VAMP2-pH, mCherry-synapsin and synaptophysin (untagged) in COS7 cells disperse reversibly upon 1,6-Hexanediol treatment. **f** Live fluorescence imaging of hippocampal neuronal cultures expressing EGFP-SCAMP5 and mCherry-synapsin, treated with 1,6-Hexanediol for 5 min and then washed. The cartoon indicates the region of the neuron examined. **g** mCherry-synapsin intensity on a presynaptic bouton and flanking axonal regions ($\pm 1.45 \mu\text{m}$ from each bouton centers) before and 1 min after addition of 1,6-Hexanediol. **h** Statistical comparison of mCherry-synapsin fluorescence intensities at the regions indicated by numbers in **g**. Values are means \pm SEM of four independent experiments (45 boutons were analyzed); $**p < 0.01$ by two-

sided paired *t*-test. **i** The localization of mCherry-synapsin before 1,6-Hexanediol treatment and after 10 min washout was analyzed. Values are means \pm SEM of three independent experiments (all boutons in a $121 \mu\text{m} \times 121 \mu\text{m}$ field were analyzed). **j** Control and 1,6-Hexanediol treated (1 min) neuronal cultures were fixed for TEM. **k** Normalized average vGlut-pH fluorescence intensity profile of presynaptic boutons stimulated with high K^+ in the presence or absence of 1,6-Hexanediol. Values are means \pm SEM of four independent experiments (160 boutons were analyzed). **l** Peak vGlut-pH fluorescence intensity values were used for statistical comparisons. Values are means \pm SD; N.S., not significant; $**p < 0.01$. Two-sided paired *t*-tests were performed on significant one-way repeated measures ANOVA (160 boutons from 4 independent experiments were analyzed). Source data are provided as a Source Data file. Scale bars, **a** and **b** = $2 \mu\text{m}$, **e** and **f** = $10 \mu\text{m}$ ($2 \mu\text{m}$ for bottom), **g** = $1 \mu\text{m}$, **j** = 500 nm . *p*-values (**d**): 9.100×10^{-5} . (**h**): 5.254×10^{-4} (left), 6.896×10^{-3} (right). (**l**): 0 (1 vs. 2), 0.7142 (1 vs. 3), 0 (2 vs. 3).

range (100 mM NaCl) supplemented with 7% PEG, the two proteins co-assembled into droplets (Fig. 3h). However, raising the salt concentration of the medium dispersed the condensates (Fig. 3h), supporting the hypothesis that low affinity, charge-based interactions between synapsin and ATG9A Ct mediate their co-assembly into droplet in living cells. When purified synapsin, the cytosolic region of synaptophysin (Synp Ct) and the cytosolic region of ATG9A (ATG9A Ct) were incubated together in the *in vitro* assay, all three proteins co-assembled together in the same droplets (Supplementary Fig. 6).

ATG9A and synaptophysin form two distinct vesicle clusters within synapsin condensates

Next, we expressed in fibroblasts ATG9A-EGFP together with synaptophysin and with mCherry-synapsin. Strikingly, ATG9A and synaptophysin segregated in distinct phases within the mCherry-synapsin phase, with synapsin being more concentrated in the synaptophysin subphase (Fig. 4a–d). CLEM analysis of cells previously exposed to CTX-HRP for 36 h further showed that both phases were represented by clusters of small vesicles labeled by the extracellular tracer (Fig. 4e). However, the vesicles in the ATG9A-EGFP/mCherry-synapsin phase were slightly bigger than the vesicles in synaptophysin/mCherry-synapsin phase [diameter: 42.0 nm (synaptophysin) vs. 55.4 nm (ATG9A)] (Fig. 4e and Supplementary Fig. 7), consistent with the different sizes of the two sets of vesicles when ATG9A and synaptophysin are expressed independently (Fig. 3d). Both components of ATG9A/synaptophysin/synapsin condensates had liquid-like properties, as shown by their property to undergo reversible dispersion by 1,6-Hexanediol (Fig. 4f; Supplementary Video 4), to fuse (Fig. 4g) and to undergo fluorescence recovery after photobleaching (Fig. 4h).

Distinct features of synaptophysin vesicles and ATG9A vesicles as revealed by proteomic analysis

The segregation of synaptophysin and of exogenous ATG9A in two distinct sets of vesicles within fibroblasts prompted us to perform a proteomic analysis to further characterize their difference. We first used proximity biotinylation, with the rationale that fusing a biotinylating enzyme to a vesicle protein would result in biotinylation of other components of the vesicle given the fluid nature of membranes. To this aim, a construct encoding miniTurboID (mTB), an enzyme that allows rapid (within minutes) labeling of neighboring proteins within a $\sim 10 \text{ nm}$ range³⁶, was fused in frame to the cytosolic C-terminus of synaptophysin and of ATG9A followed by an HA tag, and expressed in COS7 cells. An additional construct encoding an N-terminal ER targeting sequence followed by miniTurboID (expected to direct the localization of miniTurboID at the ER surface³⁶) was used as a control in initial experiments. Anti-HA tag immunofluorescence revealed that fusion of ATG9A and synaptophysin to miniTurboID-HA did not change the subcellular localization of these two membrane proteins (Supplementary Fig. 8a–c). After 15 min

incubation with exogenous biotin, biotinylated proteins were detected with streptavidin by either microscopy or Western blotting (Supplementary Fig. 8a–c and Fig. 5a, b). Most importantly, the biotinylation signal precisely overlapped with HA-tag immunoreactivity, confirming confinement of the reaction to the neighborhood of the fusion proteins (Supplementary Fig. 8a–c). Biotinylated proteins in extracts of these cells were affinity-purified by streptavidin and three biological replicates for each of the two conditions were analyzed by liquid chromatography with tandem mass spectrometry (LC/MS-MS). As illustrated in Fig. 5c, which shows the relative enrichment of biotinylated proteins in the extracts of cells expressing ATG9A-miniTurboID-HA and synaptophysin-miniTurboID-HA, respectively, numerous shared proteins were found (gray dots in Fig. 5c and Supplementary Data 1). However, substantial differences between the two biotinylated proteomes were also detected. Consistent with previous studies, ATG9A samples were enriched in subunits of AP4 (an heterotetrameric complex responsible for the sorting of ATG9A at the TGN)^{34,35,37}, in AP4 interactors (tepsin and rusc2)^{35,37,38}, in subunits of the PIKfyve complex (a phosphoinositide metabolizing complex that that function at late endosomes/lysosomes)³⁹, as well as in the autophagy factors ULK1 and ATG13⁴⁰ (Fig. 5c and Supplementary Data 1). Conversely, synaptophysin samples were enriched in proteins, or paralogues of proteins, that are found at high concentration in SVs in nerve terminals²⁷, such as Rab3, SCAMPs, vacuolar ATPase subunits, VAMP3, Rab27b, as well as other proteins implicated in SV recycling such as Bin1 (amphiphysin2)⁴¹ and synaptojanin2⁴² (Fig. 5c and Supplementary Data 1). Detection of many vacuolar ATPase subunits is consistent with the acidic pH of the lumen of synaptophysin vesicles as mentioned above (Supplementary Fig. 1d, e).

To complement results of proximity biotinylation, we next performed immunoprecipitation of the two sets of vesicles from extracts of COS7 cells expressing either synaptophysin-HA or ATG9A-HA. 25,000 g supernatants were used as starting material for these immunoprecipitations to minimize contamination of large organelles (Fig. 5d–f and Supplementary Fig. 8d–f). Quantitative LC-MS/MS of the affinity-purified vesicles (Fig. 5f and Supplementary Data 1) yielded results that aligned with those of proximity labeling (Fig. 5c and Supplementary Data 1). In spite of the use of fibroblasts as starting material, SynGO⁴³ analysis revealed enrichment in the synaptophysin vesicles of SV proteins or their paralogs (synaptogyrins, synaptotagmins, VAMP2, 3 and 7, SYPL1 and vacuolar ATPase subunits) as well as of proteins with a function in the regulation of the SV cycle (Fig. 5g and Supplementary Fig. 9). In contrast, only very few proteins were enriched in the ATG9A vesicles, relative to synaptophysin vesicles. One of them is the PIKfyve complex (Vac14, PIKfyve and Fig. 4) (Fig. 5f), in agreement with results of proximity biotinylation (Fig. 5c). Results of this proteomics analysis were validated by protein expression studies. Thus, when mCherry-tagged SV proteins (VAMP2, SCAMP5 or Rab3A) were co-expressed with ATG9A-EGFP, synaptophysin and synapsin,

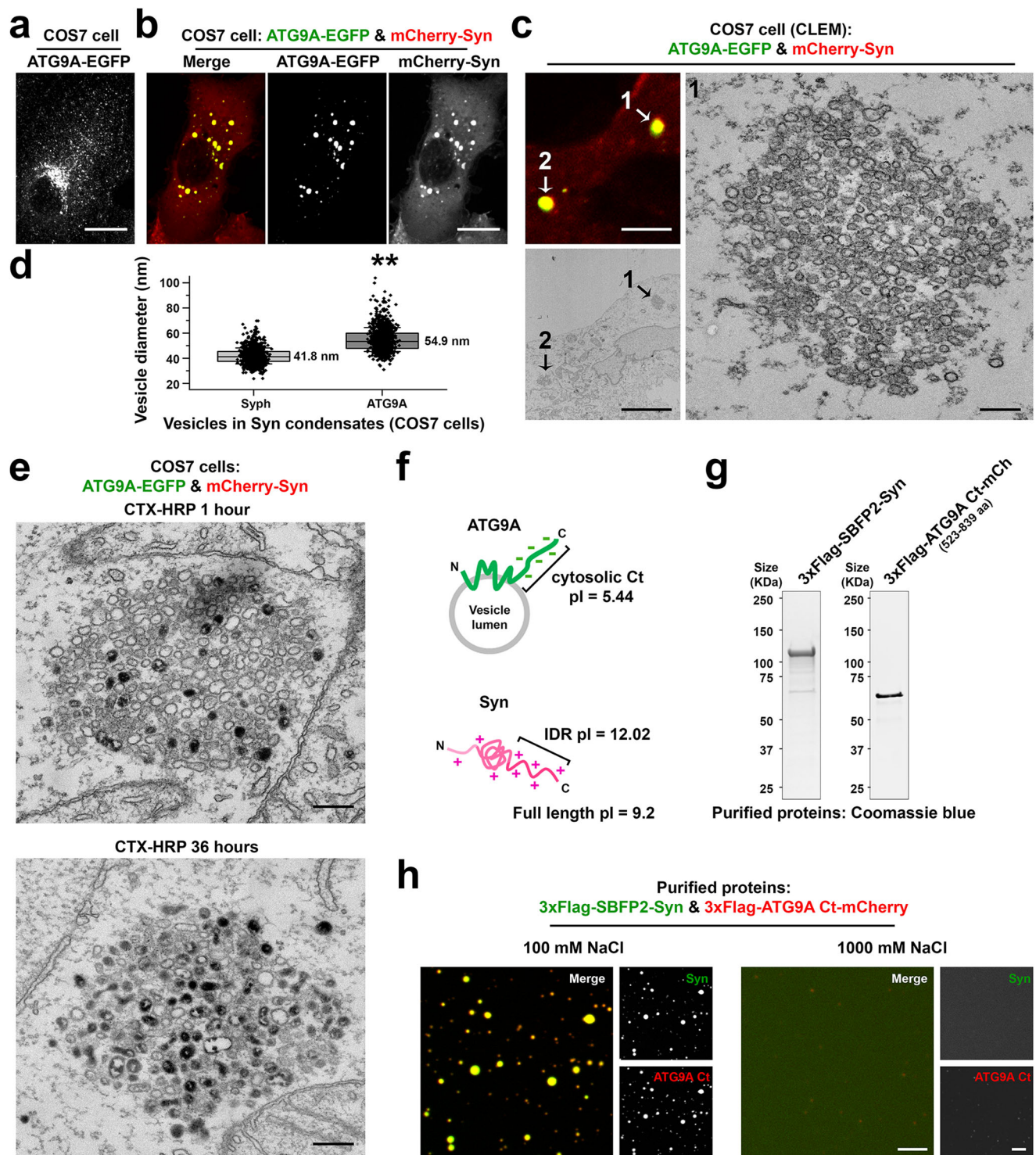


Fig. 3 | Co-expression of ATG9A-EGFP with mCherry-synapsin results in clusters of small vesicles. **a, b** ATG9A-EGFP was expressed either alone (**a**) or with mCherry-synapsin 1a (**b**) in COS7 cells. **c** Correlative light-electron microscopy (CLEM) of a COS7 cell co-expressing ATG9A-EGFP and mCherry-synapsin. Left: arrowheads point to droplets positive for ATG9A-EGFP and mCherry-synapsin in the fluorescence and EM images. Right: high-magnification EM image of droplet #1. **d** Size distribution of the ATG9A and synaptophysin vesicles when these two proteins are expressed independently with synapsin. Box plots show the median line (midline), 25/75 percentiles (boxes), and SD (whiskers). Data are represented as mean \pm SD. 1000 vesicles were measured for each group (from three independent experiments). $**p < 0.01$, by two-sided Student's *t*-test. **e** COS7 cells co-expressing ATG9A-EGFP and mCherry-synapsin were treated with 10 μ g/ml cholera toxin conjugated

HRP (CTX-HRP) for either 1 h (left) or 36 h (right) at 37 $^{\circ}$ C and then fixed for TEM. **f** Schematic drawing of synapsin and ATG9A. pI = isoelectric point. IDR: intrinsically disordered region (C-terminal region of synapsin). **g** N-terminal 3xFlag conjugated SBFP2-synapsin (full length) and ATG9A Ct (C-terminal region only: 523–839 aa)-mCherry were purified from Expi293 cells and analyzed by SDS-PAGE and Coomassie Blue staining. **h** Co-assembly of purified synapsin and of purified ATG9A Ct into liquid droplets. 3xFlag-SBFP2-synapsin (7.5 μ M) and 3xFlag-ATG9A Ct-mCherry (2 μ M) were mixed in a buffer containing 25 mM Tris-HCl (pH 7.4), 0.5 mM TCEP, 7% PEG and either 100 mM or 1000 mM NaCl. Increasing the concentration of NaCl resulted in the dispersion of the droplets. Source data are provided as a Source Data file. Scale bars, **a** and **b** = 20 μ m, **c** = 5 μ m (left) or 200 nm (right), **e** = 200 nm, **h** = 5 μ m. *p*-value (**d**): 4.109×10^{-5} .

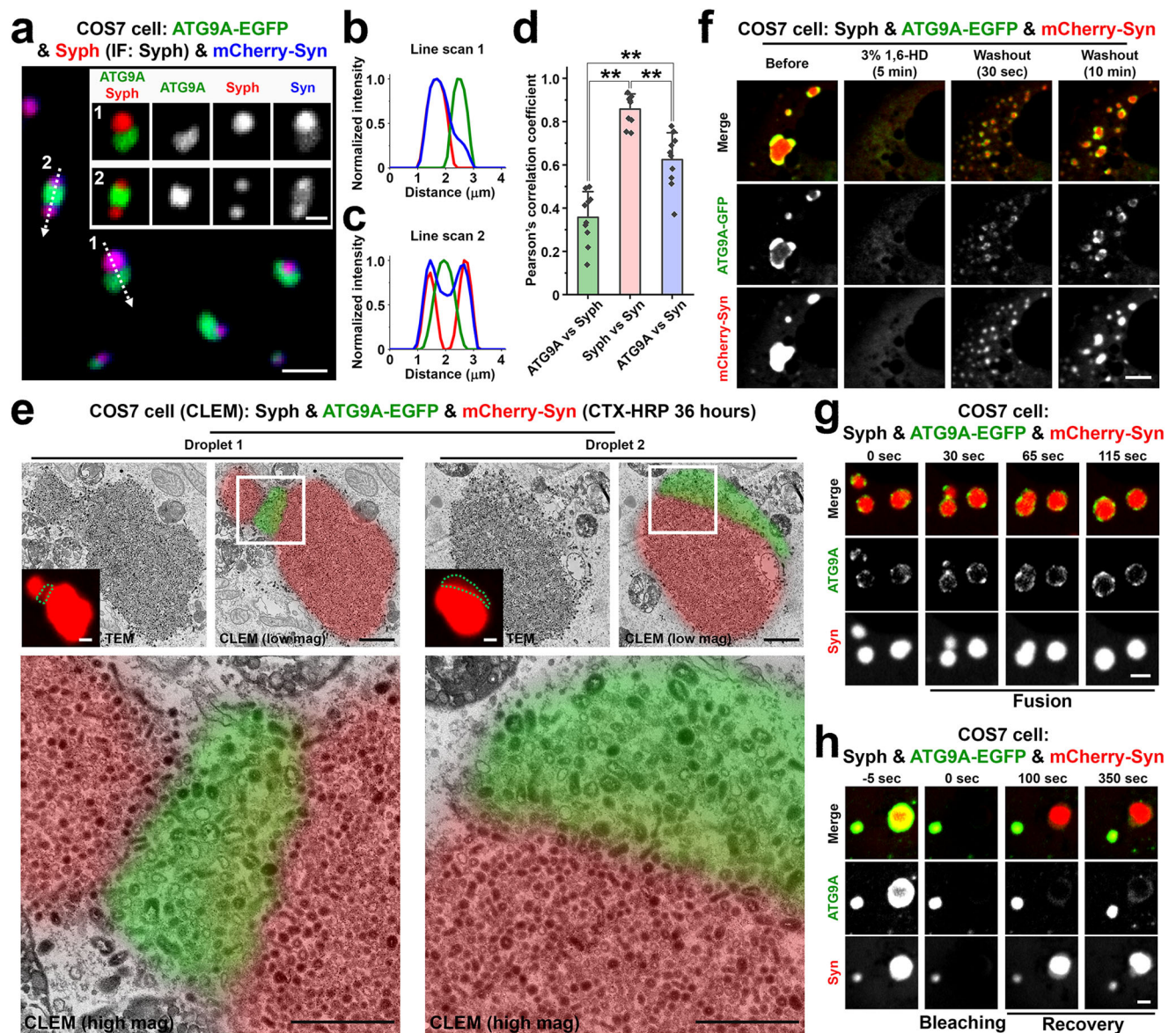


Fig. 4 | Synaptophysin and ATG9A segregate in distinct vesicle clusters within the synapsin phase. COS7 cells were triple co-transfected with synaptophysin (untagged), ATG9A-EGFP and mCherry-synapsin. **a–c** Representative confocal image (**a**), and corresponding line-scan analysis of the droplets (**b**, **c**) showing that synapsin phases include two distinct subphases containing synaptophysin and ATG9A-EGFP, respectively. Synaptophysin was visualized by immunofluorescence. The intensity of the mCherry-synapsin fluorescence is more intense on the synaptophysin phase, as quantified in **d**. **d** The colocalization of the pairs of proteins indicated was calculated by Pearson's coefficients. Values are means \pm SD. $^{**}p < 0.01$ by one-way ANOVA with Tukey's HSD post hoc test (droplets in 10 different cells were analyzed). **e** Synaptophysin, ATG9A-EGFP and mCherry-synapsin co-

expressing COS7 cells were incubated with 10 μ g/ml cholera toxin conjugated HRP (CTX-HRP) for 36 h and then fixed for correlative light-electron microscopy (CLEM). Green dotted lines in the insets indicate ATG9A-EGFP-positive regions in mCherry-synapsin condensates. Note that synaptophysin and ATG9A vesicles have slightly different sizes. **f–h** Dynamics of the ATG9A, synaptophysin and synapsin droplets: **f** Reversible dispersion by 1,6-Hexanediol treatment. See also Supplementary Video 4; **g** fusion; **h** Fluorescence recovery after photobleaching. Source data are provided as a Source Data file. Scale bars, **a** = 2 μ m (1 μ m for insets), **e** = 1 μ m (low mag and inset) or 500 nm (high mag), **f** = 5 μ m, **g** and **h** = 2 μ m. *p*-values (**d**): 0 [(ATG9A vs. Syph) vs. (Syph vs. Syn)], 2.009×10^{-5} [(ATG9A vs. Syph) vs. (ATG9A vs. Syn)], 1.270×10^{-4} [(Syph vs. Syn) vs. (ATG9A vs. Syn)].

they were enriched in the synaptophysin subphase within the synapsin phase (Fig. 6). Conversely, VAC14 was enriched in the ATG9A subphase (Fig. 6).

ATG9A has a conserved YXX Φ E motif (YQRLE) in its N-terminal cytosolic region (Fig. 7a), which is required for ATG9A exit from the trans-Golgi network (TGN) by mediating capture of ATG9A into AP4 coated buds³⁴. Accordingly, AP4-binding defective ATG9A mutant (ATG9A^{YSA}) massively accumulated at the TGN, at a position well separated by the cis-Golgi marker GMI30, where it precisely colocalized with the TGN marker TGN46 and failed to form sparse cytoplasmic droplets in the presence of mCherry-synapsin (Fig. 7b and

Supplementary Video 5). In fact, when synapsin was co-expressed with ATG9A^{YSA}, it accumulated together with ATG9A^{YSA} in the TGN area (Fig. 7c), confirming its property to co-assemble with ATG9A. CLEM analysis further revealed that this accumulation of mutant ATG9A and TGN46 correlated with a striking accumulation of small heterogeneously sized vesicles (Fig. 7c).

Surprisingly, when ATG9A^{YSA}-EGFP was expressed with both mCherry-synapsin and synaptophysin, it was not retained in the TGN and precisely colocalized with synaptophysin and synapsin in droplets (vesicle condensates) sparse around the cytosol (Fig. 7d–f). We suggest that under these conditions ATG9A^{YSA}-EGFP follows a default pathway

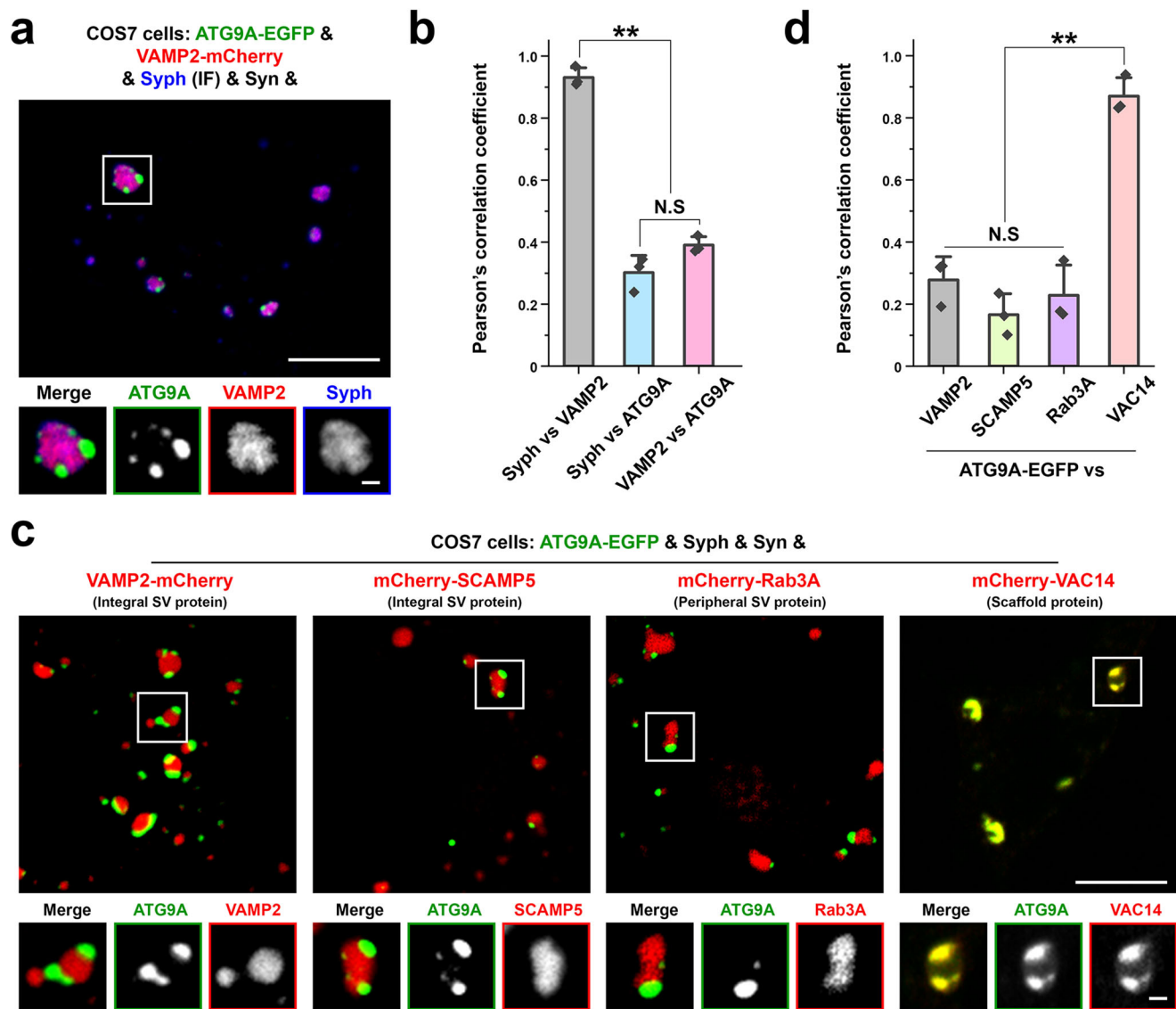


Fig. 6 | Validation of the proteomic analysis of ATG9A and synaptophysin vesicles. **a** Segregation of VAMP2-mCherry from ATG9A-EGFP in COS7 cells also expressing synapsin and synaptophysin. Synaptophysin was visualized by immunofluorescence. **b** The colocalization of the pairs of proteins indicated was calculated by Pearson's coefficients. Values are means \pm SD; N.S., not significant; $**p < 0.01$ by one-way ANOVA with Tukey's HSD post hoc test (droplets in 3 different cells were analyzed). **c** ATG9A is segregated from SV proteins (VAMP2, SCAMP5, Rab3A) but precisely colocalizes with VAC14 in COS7 cells also expressing synaptophysin and synapsin, consistent with proteomics data. **d** The colocalization of the

pairs of proteins indicated was calculated by Pearson's coefficients. Values are means \pm SD; N.S., not significant; $**p < 0.01$ by one-way ANOVA with Tukey's HSD post hoc test (droplets in 3 different cells for each condition were analyzed). Source data are provided as a Source Data file. Scale bars, **a** and **c** = 10 μ m (1 μ m for high-magnification images). *p*-values (**b**): 3.032×10^{-6} [(Syph vs. VAMP2) vs. (Syph vs. ATG9A)], 7.549×10^{-6} [(Syph vs. VAMP2) vs. (VAMP2 vs. ATG9A)], 0.07488 [(Syph vs. ATG9A) vs. (VAMP2 vs. ATG9A)], 0.3406 (VAMP2 vs. SCAMP5), 0.8552 (VAMP2 vs. Rab3), 5.655×10^{-5} (VAMP2 vs. VAC14), 0.7519 (SCAMP5 vs. Rab3A), 1.546×10^{-5} (SCAMP5 vs. VAC14), 3.116×10^{-5} (Rab3A vs. VAC14).

and that the interaction of ATG9A with AP4 is needed to sort ATG9A away from this pathway.

ATG9A in nerve terminals

We next examined the localization of ATG9A-EGFP relative to SV proteins in nerve terminals. When ATG9A-EGFP was co-expressed with synaptophysin-HA in cultured hippocampal neurons, the two proteins accumulated at distinct, although juxtaposed, spots at presynaptic sites (Fig. 8a, b). On the contrary, mCherry-SCAMP5 precisely colocalized with synaptophysin-HA at these sites (Fig. 8a, b). When ATG9A-EGFP, mCherry-synapsin and synaptophysin-HA were co-expressed together, the juxtaposed spots of ATG9A-EGFP and of synaptophysin-HA were both positive for synapsin as we had observed in fibroblasts (Fig. 4a), although, again as in fibroblasts, synapsin was more concentrated in the synaptophysin-region (Fig. 8c). Similar results were

observed by examining the localization of the endogenous proteins by immunofluorescence. ATG9A immunoreactivity was juxtaposed to, but not overlapping with, the immunoreactivities of synaptophysin, VAMP2 and Rab3A, which precisely colocalized (Fig. 8d–g).

AP4-binding defective ATG9A-EGFP (ATG9A^{V8A}-EGFP) was also present in nerve terminals (Supplementary Fig. 10a), indicating that in neurons a pool of ATG9A can exit the TGN, at least under these conditions that lead to overexpression. However, in contrast to WT ATG9A-EGFP, ATG9A^{V8A}-EGFP colocalized with the SV marker SCAMP5, supporting the importance of AP4 binding for its segregation from synaptophysin in both fibroblasts (Fig. 7d–f) and neurons (Supplementary Fig. 10a, b). As previously reported^{44–46}, we found that the level of ATG9A was increased in AP4E1 knockout (AP4E1 KO) mouse brains, where the bulk of ATG9A remains confined to cell bodies, while levels of SV proteins (synaptophysin and VAMP2) were unchanged

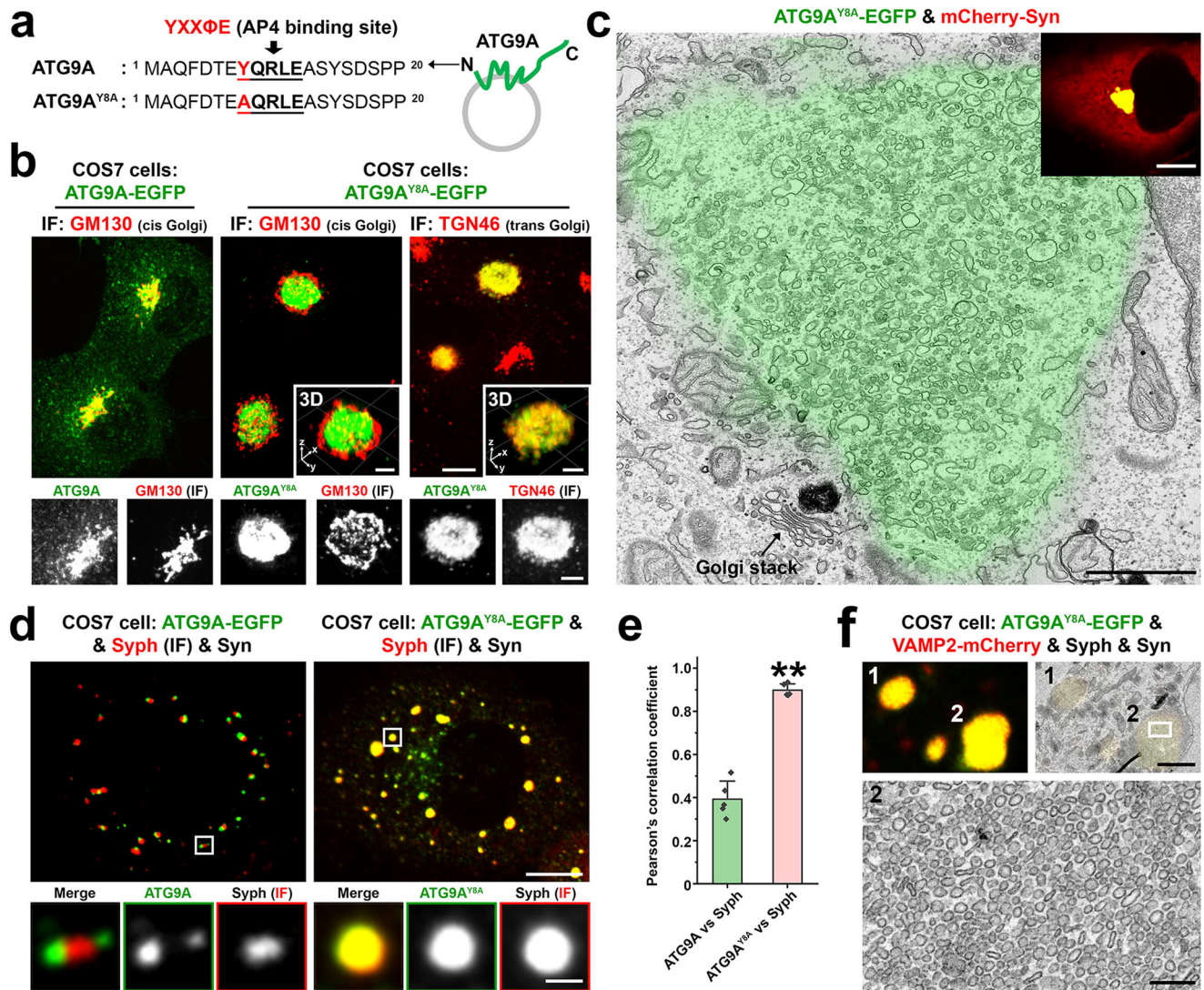


Fig. 7 | Impact of the Y8A mutation of ATG9A on its sorting and segregation from synaptophysin. **a** Amino acid sequence of the cytosolic N-terminal region of ATG9A with the AP4-binding motif in bold characters. **b** COS7 cells expressing ATG9A-EGFP (WT) or ATG9A^{Y8A}-EGFP and immunostained for cis-Golgi (GM130) and trans-Golgi (TGN46) markers, showing that ATG9A^{Y8A} is retained in the TGN area, where it colocalizes with TGN46. See also Supplementary Video 5. **c** Correlative light-electron microscopy (CLEM) of a COS7 cell expressing ATG9A^{Y8A}-EGFP and mCherry-synapsin, showing that the accumulation of ATG9A^{Y8A} in the TGN area (green color from the fluorescence image) correlates with a massive accumulation of small heterogeneously sized vesicular-tubular structures in the same area. An arrow points to a Golgi stack. The inset shows that synapsin is colocalized with ATG9A^{Y8A} in the TGN area, while no sparse droplets positive for ATG9A^{Y8A} and for synapsin are present in this cell. **d** COS7 cell triple transfected with synapsin,

synaptophysin and either ATG9A-EGFP or ATG9A^{Y8A}-EGFP. Synaptophysin was detected by immunofluorescence. ATG9A^{Y8A}-EGFP failed to form distinct clusters within synapsin condensates and completely intermixed with synaptophysin. **e** Colocalization analysis of synaptophysin vs. either ATG9A (WT) or ATG9A^{Y8A} in COS7 cells also expressing synapsin. Values are means \pm SD. ****** $p < 0.01$ by the two-sided Student's *t*-test (droplets in 5 cells for each condition were analyzed). **f** CLEM image of a COS7 cell quadruple transfected with ATG9A^{Y8A}-EGFP, VAMP2-mCherry, synaptophysin and synapsin. Top images show corresponding light microscopy and EM fields and the bottom image shows a detail of droplet #2 at high magnification. Source data are provided as a Source Data file. Scale bars, **b** = 10 μ m (5 μ m for insets and enlarged images), **c** = 1 μ m (10 μ m for inset), **d** = 10 μ m (1 μ m for enlarged images), **f** = 2 μ m (200 nm for the enlarged image at the bottom). *p*-value (**e**): 1.322×10^{-6} .

(Supplementary Fig. 10c, d). However, we also found that the pool of ATG9A present in vesicles immunisolated by anti-VAMP2 antibodies was increased, confirming a leakage of ATG9A into SVs. (Supplementary Fig. 10e–h).

Discussion

Results of this study show that the generation of SV-like organelles in fibroblasts is a powerful experimental system to gain insight into mechanisms of SV biogenesis and clustering. We had previously shown that even in this exogenous system SV proteins can self-organize into small vesicles that share several characteristic properties with bona fide SVs such as similarity in size, property to undergo exo-endocytosis

and clustering by synapsin into a liquid phase¹⁵. We now demonstrate that all of several exogenous SV proteins tested co-assemble with exogenous synaptophysin in these vesicles and that synaptophysin is the critical driver of these assemblies, at least in this exogenous system. This finding opens the possibility of using this system to gain new insight into the still open question of how SV proteins co-assemble into such a specialized vesicle.

We show that ATG9A accumulates in a different class of slightly larger vesicles, although even such vesicles can be captured in the synapsin phase. The different protein composition of the two types of vesicles, as revealed by a proteomic analysis, further demonstrates that they are part of two distinct vesicle traffic pathways. The list of

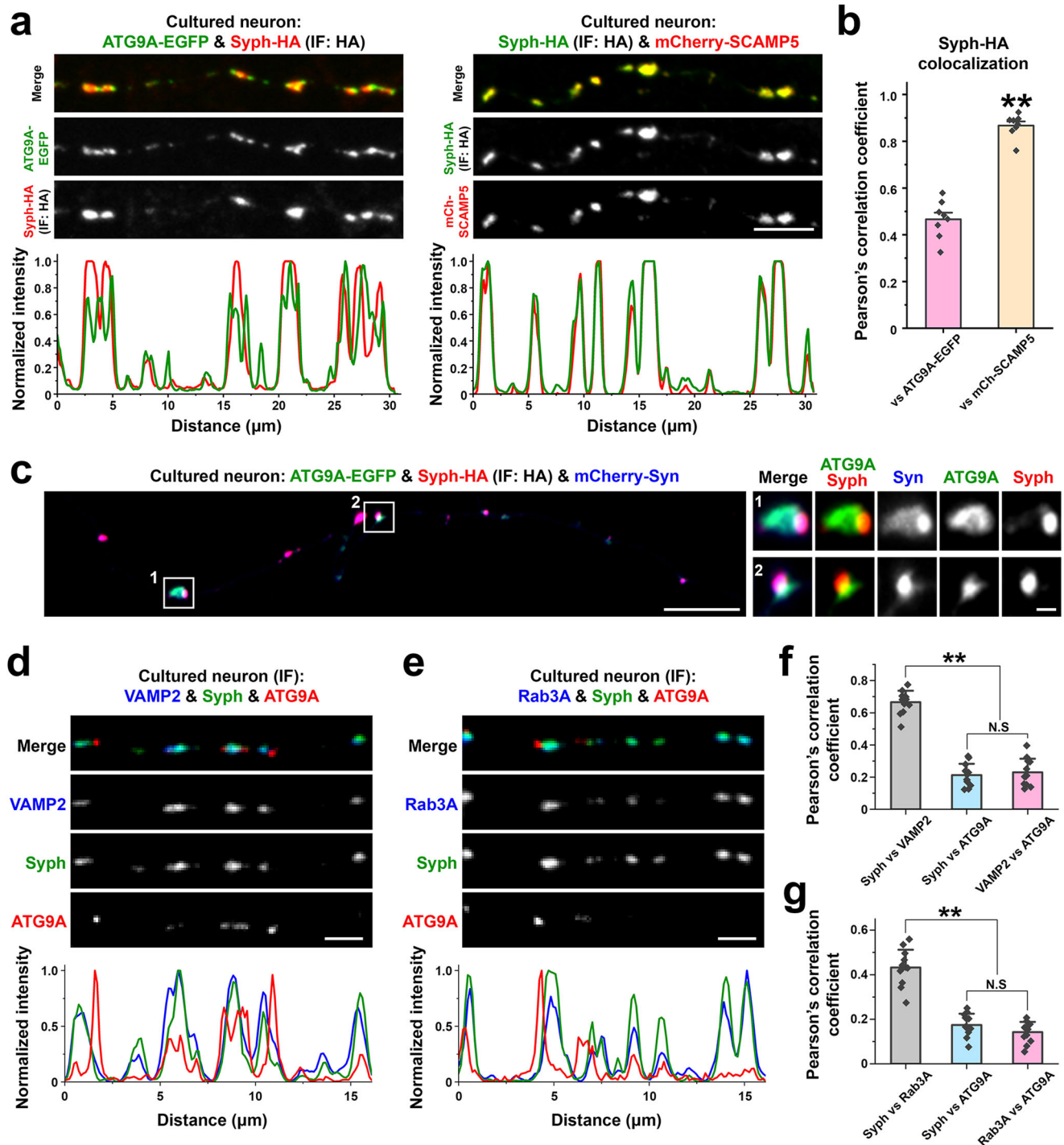


Fig. 8 | **ATG9A vesicle localization in neurons.** **a–c** Mouse hippocampal neuronal cultures were transfected as indicated and imaged at DIV14–17. **a** Representative confocal images (top), and corresponding line-scan analysis (bottom) of neuronal cultures expressing synaptophysin-HA with ATG9A-EGFP or mCherry-SCAMP5. Synaptophysin-HA was detected by anti-HA immunofluorescence. **b** Colocalization analysis calculated by Pearson's coefficients. Values are means \pm SEM. ** $p < 0.01$ by the two-sided Student's *t*-test (all boutons in 8 field of view ($121 \mu\text{m} \times 121 \mu\text{m}$) for each condition from two independent cultures were quantified). **c** Localization of ATG9A-EGFP, synaptophysin-HA and mCherry-synapsin in presynaptic varicosities of an axon. Synaptophysin-HA was visualized by anti-HA immunofluorescence. **d–g** Mouse hippocampal neuronal cultures were fixed and stained as indicated at DIV14–17 to visualize endogenous localization of ATG9A in neurons.

d, e Representative confocal images showing immunoreactivity for endogenous ATG9A, synaptophysin and VAMP2 (**d**) or Rab3A (**e**) in cultured hippocampal neurons. Corresponding line-scans are shown at the bottom. **f, g** Colocalization analysis. Values are means \pm SD; N.S., not significant; ** $p < 0.01$ by one-way ANOVA with the Tukey's HSD post hoc test (12 images ($121 \mu\text{m} \times 121 \mu\text{m}$) for each) from two independent cultures were analyzed). Source data are provided as a Source Data file. Scale bars, **a** = $5 \mu\text{m}$, **c** = $10 \mu\text{m}$ ($1 \mu\text{m}$ for high-magnification images), **d** and **e** = $2 \mu\text{m}$. *p*-values (**b**): 9×10^{-9} , (**f**): 0 [(Syph vs. VAMP2) vs. (Syph vs. ATG9A)], 0 [(Syph vs. VAMP2) vs. (VAMP2 vs. ATG9A)], 0.8080 [(Syph vs. ATG9A) vs. (VAMP2 vs. ATG9A)]. (**g**): 0 [(Syph vs. Rab3A) vs. (Syph vs. ATG9A)], 0 [(Syph vs. Rab3A) vs. (Rab3A vs. ATG9A)], 1.826 [(Syph vs. ATG9A) vs. (Rab3A vs. ATG9A)].

endogenous proteins that co-enrich with synaptophysin vesicles in COS7 cells supports the hypothesis that SVs represent a special adaptation of a house-keeping vesicle recycling endocytic pathway, as several such proteins are also components of SVs or their paralogues. On the other hand, the enrichment of endogenous proteins implicated in lysosome function (PIKfyve complex³⁹) and autophagy (ULK1 complex⁴⁰) in ATG9A vesicles is in line with a role of this protein in protein degradation.

Another important result of our study is that the rapid and reversible dispersion of synapsin-dependent SV-like condensates observed in fibroblasts upon addition of 1,6-Hexanediol is phenocopied in axon terminals. This finding adds a missing piece of evidence to the concept that native SV clusters are organized according to liquid-liquid phase separation principles. The dispersion-reclustering correlates with a strong difference in depolarization evoked SV induced by high K⁺, consistent with the expectation that SV clustering at presynaptic sites plays a critical role in allowing a sustained secretory response to massive stimulation. Dispersion of active zone proteins⁴⁷ may contribute to the effect of 1,6-Hexanediol on secretion, as phase separation principles were proposed to contribute also to the assembly of many such proteins, including RIM, RIM-BP, ELKS, and liprin- α ^{48–51}.

Presynaptically localized ATG9A was recently shown to undergo activity-dependent exo-endocytosis in parallel with SV proteins in *C. elegans*^{23,25}. However, consistent with our present findings, even in worms ATG9A did not appear to precisely colocalize with SVs: (1) its localization clearly diverged from the localization of SVs after perturbation of endocytosis^{23,25} and (2) the localization of SV proteins and of ATG9A was differentially affected by genetic perturbation of the active/periaxial zone protein Clarinet²⁵. Moreover, while mass spectrometry analysis of purified SV fraction from rat brain detected ATG9A in such vesicles^{26–28}, the amount of ATG9A detected was extremely low²⁷. It was estimated that 4 copies of ATG9A were present in 100 vesicles²⁷. Considering that ATG9A occurs as a trimer, there would be only 1–2 ATG9A trimers per 100 vesicles in presynaptic nerve terminals (vs. 525 synaptophysin hexamers per 100 SVs)^{27,29}. Thus, these findings are consistent with a segregation of ATG9A from bona fide SVs. The concentration of ATG9A in small vesicles is in line with evidence that ATG9A has curvature promoting properties²². A propensity to generate or assemble into vesicles larger than bona fide SVs could in principle contribute to its segregation from synaptophysin vesicles. However, we show here that the segregation of ATG9A from synaptophysin occurs only if ATG9A can bind AP4, an adaptor protein shown to be required for the sorting of ATG9A at the TGN. An ATG9A construct lacking the AP4-binding site can surprisingly exit the TGN if co-expressed with synaptophysin, and precisely colocalizes with synaptophysin vesicle clusters both in fibroblasts and in nerve terminals.

The property of ATG9A vesicles to be clustered with synapsin both in fibroblasts and, as shown in Fig. 8, also in nerve terminals was unexpected. As discussed above in Results, this property likely relies on the negative charge of the cytosolic C-terminal region of ATG9A, which similarly to the negatively charged C-terminal tail of synaptophysin, interacts with the basic C-terminal region of synapsin. However, ATG9A and synaptophysin vesicles segregate in different subphases within the synapsin phase. Mechanisms that may contribute to this difference may include a different affinity for synapsin, a different concentration of binding sites for synapsin on the ATG9A vesicles or the different diameter of synaptophysin and ATG9A vesicles.

Collectively, our study demonstrates that, both in nerve terminals and in an exogenous system, major SV proteins and of ATG9A are differentially sorted and represents an important step towards the elucidation of how SV traffic and vesicle traffic responsible for autophagosome formation are interconnected.

Methods

Plasmid DNA construction

Human ATG9A was amplified from pMXs-puro-RFP-ATG9A from Addgene (plasmid #60609) and subcloned into the EGFP-N1 vector. ATG9A^{Y8A}-EGFP was generated using site-directed mutagenesis (QuikChange II XL, Agilent Technologies) of ATG9A-EGFP. The following plasmids were previously described: Synaptophysin¹⁵, mCherry-synapsin 1a¹⁵, EGFP-SCAMP5⁵², Synaptotagmin1-EGFP³⁰, mCherry-Rab3A⁵³, and mRFP-Rab5A⁵³. EGFP-synapsin 2a was generated in our laboratory. The synapsin 3a construct was purchased from GenScript and subcloned into the mCherry-C1 vector. Synapsin 1a full length, cytosolic C-terminal region of synaptophysin (219–308 aa) and ATG9A (523–839 aa) were amplified by PCR and subcloned into the SBFP2-C1, EGFP N1 or mCherry-N1 vectors respectively and then moved into the p3xFlag-CMV10 vector for protein purification. Synaptophysin-HA or ATG9A-HA constructs were generated by inserting the HA epitope sequence at the C-terminus of the synaptophysin or ATG9A sequences. miniTurboID was amplified from Addgene (plasmid #107174) and inserted between synaptophysin and the HA tag or between ATG9A and the HA tag to obtain synaptophysin-miniTurboID-HA and ATG9A-miniTurboID-HA. The HA tag and a stop codon were inserted between miniTurboID and the V5 tag of Addgene plasmid #107174 to generate ER-miniTurboID-HA. Rab3A was amplified by PCR from the mCherry-Rab3A⁵³ and cloned into the EGFP-C1 vector to construct EGFP-Rab3A. Human VAC14 was obtained from Addgene (Plasmid #47418) and subcloned into the mCherry-C1 vector. The following plasmids were kind gift: Transferrin receptor-pHluorin (from Dr. David Zenisek, Yale University), VAMP2-pHluorin (from Dr. James Rothman, Yale University), vGlut-pHluorin (from Dr. John Rubenstein, University of California San Francisco), vGAT-pHluorin (from Dr. Susan Voglmaier, University of California San Francisco). Each construct was validated by DNA sequencing.

Antibodies

The following primary antibodies were used: anti-synaptophysin (101002, Synaptic Systems; 101011, Synaptic Systems; 101308, Synaptic Systems; 1:500 for IF, 1:3000 for WB), anti-VAMP2 (104211, Synaptic Systems; 1:70 for IP, 1:500 for IF or 1:3000 for WB), anti-Rab3A (107111, Synaptic Systems; 1:1000 for IF), anti-ATG9A (ab108338, Abcam; 1:500 for IF or 1:3000 for WB), anti-LC3 (PM036, MBL; 1:3000 for WB), anti-AP4E1 (612018, BD Transduction Laboratories™; 1:2000 for WB), anti-Actin (691002, MP Biomedicals; 1:3000 for WB), anti-HA (G246, Covance; 1:1000 for IF or 1:2000 for WB), anti-GM130 (610822, BD Bioscience; 1:500 for IF or 1:1,000 for WB), anti-TGN46 (AHP500GT, AbD Serotec; 1:1000 for IF) and anti-TOMM40 (18409-1-AP, Proteintech; 1:3000 for WB). The following secondary antibodies were used for immunofluorescence (IF, 1:1000): Alexa Fluor 488 anti-mouse IgG (A11001, Invitrogen), Alexa Fluor 594 anti-mouse IgG (A21203, Invitrogen), Alexa Fluor 647 anti-mouse IgG (A32787, Invitrogen), Alexa Fluor 594 anti-rabbit IgG (A11037, Invitrogen), Alexa Fluor 647 anti-sheep IgG (A21448, Invitrogen), Alexa Fluor 488 anti-guinea pig IgG (A11073, Invitrogen). Alexa Fluor 647 conjugated Streptavidin (S32357, Invitrogen, 1:1000) was used to stain biotinylated proteins. The following secondary antibodies were used for Western blotting (WB, 1:15000): IRDye 800CW anti-mouse (926-32210, LI-COR), IRDye 800CW anti-rabbit (926-32211, LI-COR), IRDye 800CW anti-guinea pig (925-32411, LI-COR), IRDye 680LT anti-mouse (926-68020, LI-COR) and IRDye 680LT anti-rabbit (926-68021, LI-COR). IRDye 680RD Streptavidin (926-68079, LI-COR, 1:3000) was used to detect biotinylated proteins.

Cell culture and transfection

COS7 cells were grown in DMEM supplemented with 10% FBS, 100 U/ml penicillin and 100 mg/ml streptomycin. Cells were maintained at 37°C in a 5% CO₂ humidified incubator and were transfected by

Lipofectamine-2000. Hippocampal neurons were cultured from post-natal day 0 C57BL/6 (B6) mouse pups of either sex and transfected at 8 days in vitro (DIV) using a calcium phosphate transfection method. Neurons were used at days in vitro (DIV) 14 to 18. All animal experiments were approved by the Institutional Animal Care and Use Committee of Yale University. The mouse colony was maintained in the vivarium with a 12 h light/dark cycle, stable temperature at $22\text{ }^{\circ}\text{C} \pm 1\text{ }^{\circ}\text{C}$, and humidity between 20 and 50%.

Correlative light and electron microscopy (CLEM)

COS7 cells were plated on 35 mm gridded, glass-bottom MatTek dish (P35G-1.5-14-CGRD) and transfected as indicated. Cells with/without CTX-HRP (10 $\mu\text{g}/\text{ml}$, Invitrogen, C34780) incubation were fixed with 4% PFA in 0.1 M phosphate buffer (pH 7.3) (PB) and washed in PB. Regions of interest were selected by confocal fluorescence microscopy and their coordinates were identified using phase contrast. Cells were further fixed with 2.5% glutaraldehyde in 0.1 M sodium cacodylate buffer, postfixed in 2% OsO_4 and 2% $\text{K}_4\text{Fe}(\text{CN})_6$ (Sigma-Aldrich, St. Louis, MO) in 0.1 M sodium cacodylate buffer, *en bloc* stained with 2% aqueous uranyl acetate, dehydrated, and embedded in Embed 812. The HRP reaction was carried out with diaminobenzidine (Sigma, D-5637) (0.5 mg/ml) and H_2O_2 (JT Baker, 2186-01) (0.01%) in 0.1 M ammonium phosphate buffer (pH 7.4) after the glutaraldehyde fixation step. Regions of interest were relocated based on the pre-recorded coordinates, sectioned and imaged. Ultrathin sections (50–60 nm) were observed in a Talos L120C TEM microscope at 80 kV. Images were taken with Velox software and a $4\text{ k} \times 4\text{ K}$ Ceta CMOS Camera (Thermo Fisher Scientific). Except when noted, all EM reagents are from EMS, Hatfield, PA.

Fluorescence imaging

Cells were imaged with a spinning disk confocal microscope using a planar Apo objective 60x, 1.49-NA and an EM-CCD camera (C9100-50; Hamamatsu Photonics) under the control of Improvision UltraVIEW VoX system (PerkinElmer). Live-cell imaging buffer (Invitrogen) was used for live-cell imaging of COS7 cells. For 1,6-Hexanediol experiments, cells were briefly washed in live-cell imaging buffer, incubated with 3% 1,6-Hexanediol in live-cell imaging buffer and then returned to live-cell imaging buffer alone. For live imaging of neurons, neuronal cultures were switched from neurobasal medium to Tyrode buffer (136 mM NaCl, 2.5 mM KCl, 2 mM CaCl_2 , 1.3 mM MgCl_2 , 10 mM HEPES and 10 mM glucose). 3% 1,6-Hexanediol was added to this medium as indicated and stimulation was performed by replacing 136 mM NaCl, 2.5 mM KCl with 78.5 mM NaCl, 60 mM KCl. Unless specified otherwise, time-lapse images were acquired every 5 s. For FRAP experiment of vesicle condensates, a single droplet was bleached by scanning with a 488 nm laser for 1 sec and fluorescence recovery was subsequently imaged at 5 s intervals.

Immunofluorescence

COS7 cells or cultured hippocampal neurons were fixed with 4% PFA in 4% sucrose containing PB for 15 min at RT and washed in PBS. After fixation, cells were incubated with blocking buffer (3% BSA and 0.2% triton X-100 in PBS) for 30 min at RT. Subsequent primary and Alexa Fluor-conjugated secondary antibody incubations were made in this buffer. Samples were finally mounted in Prolong Gold (Invitrogen).

Protein purification and in vitro phase separation assays

Constructs encoding 3xFlag-SBFP2-synapsin, 3xFlag-Syph Ct-EGFP or 3xFlag-ATG9A Ct-mCherry were transfected into Expi293F cells (Thermo Fisher Scientific) according to manufacturer instructions. Proteins were expressed for three days following induction. Cells were harvested by centrifugation and lysed by 3 freeze-thaw cycles in lysis buffer that contained 25 mM Tris 7.4, 500 mM NaCl, 10% Glycerol, 2 mM DTT and complete EDTA-free protease inhibitor cocktail

(Roche). Cellular debris were removed by centrifugation at $15,000 \times g$ for 1 h at $4\text{ }^{\circ}\text{C}$, and the clarified lysate was mixed with anti-FLAG M2 resin (Sigma) for 2 h while rotating at $4\text{ }^{\circ}\text{C}$. The resin was then washed with 3×10 bed volumes of lysis buffer and eluted with 800 μl (for 60 ml of cell suspension) lysis buffer supplemented with 0.2 mg/ml 3xFlag peptides (Sigma). The purity of the proteins was assessed by SDS-PAGE. Purified proteins were dialyzed overnight at $4\text{ }^{\circ}\text{C}$ against a buffer containing 25 mM Tris 7.4, 100 mM NaCl, 0.5 mM TCEP. After dialysis proteins were further clarified by centrifugation at $17,000 \times g$ for 10 min at $4\text{ }^{\circ}\text{C}$ and used for the following phase separation experiments. Protein mixtures were prepared in a PCR tube at concentrations as indicated in the presence of 7% PEG 8k. Immediately after preparation, samples were deposited (6–10 μl) on 35-mm glass-bottom dishes (MatTek Corp). Images were captured with a Spinning disk confocal (SDC) at RT.

Proximity biotinylation

COS7 cells expressing the indicated constructs were plated, transfected, and labeled with pre-warmed biotin containing complete DMEM medium (500 μM biotin) for 15 min at $37\text{ }^{\circ}\text{C}$. Cells were then washed five times with ice-cold PBS, and lysed with lysis buffer (20 mM Tris-HCl, pH 8, 1% triton X-100, 10% glycerol, 137 mM NaCl, 2 mM EDTA, 1 mM PMSF, 10 mM leupeptin, 1.5 mM pepstatin, and 1 mM aprotinin). Lysates were centrifuged at $14,000 \times g$ for 20 min at $4\text{ }^{\circ}\text{C}$ and the supernatants were collected. Protein concentration was estimated with the Pierce BCA protein Assay kit (Thermo Scientific, MA). Lysates containing 1.2 mg protein for sample were then incubated overnight under rotation at $4\text{ }^{\circ}\text{C}$ with streptavidin-coated magnetic beads (Pierce) pre-washed twice with lysis buffer. The beads were subsequently washed three times with lysis buffer, additional three times with PBS to remove the detergent and resuspended in 1.2 ml PBS in Eppendorf tubes. 1 ml aliquots of this suspensions were then transferred to new Eppendorf tubes, the supernatants were removed, and the beads were frozen with dry ice for LC-MS/MS analysis. The remaining portions of the samples (0.2 ml) were used to verify the enrichment of biotinylated proteins. Biotinylated proteins were eluted from the beads by boiling for 10 min in 3x sample buffer (165 mM Tris pH 6.8, 17% glycerol, 5% SDS, 0.045% DTT and 0.06% bromophenol blue) supplemented with 20 mM DTT and 2 mM biotin. Eluted proteins were processed for SDS-PAGE and Western blotting. To verify the occurrence of biotinylation at the expected sites, COS7 cells were incubated with 500 μM biotin for 15 min at $37\text{ }^{\circ}\text{C}$ prior to fixation, then washed five times with PBS and incubated with blocking buffer for 30 min at RT. Finally, cells were incubated with Alexa Fluor-conjugated HA and streptavidin antibodies in blocking buffer to detect localization of mini-TurboID fusion proteins and biotinylated proteins.

Vesicle immunoisolation

Cells expressing HA-tagged proteins were washed twice with PBS, scraped into ice-cold homogenization buffer (5 mM Tris, 250 mM Sucrose, 1 mM EGTA pH 7.4) and disrupted by 15 passages through a 27-gauge syringe on ice. The homogenate was centrifuged at $1000 \times g$ for 10 min at $4\text{ }^{\circ}\text{C}$. The supernatant was collected (PNS, postnuclear supernatants) and ultracentrifuged at $25,000 \times g$ for 20 min $4\text{ }^{\circ}\text{C}$ (or $50,000 \times g$ for 30 min $4\text{ }^{\circ}\text{C}$) in a Beckman TLA100.3 rotor (Optima™ TLX Ultracentrifuge, Beckman). The pellet was discarded, and the supernatant was mixed with HA magnetic beads (Pierce) that had been washed twice with homogenization buffer. This mixture was incubated overnight at $4\text{ }^{\circ}\text{C}$. Subsequently beads were washed three times with homogenization buffer, three times with PBS and frozen in dry ice for LC-MS/MS analysis.

Mass spectrometry analyses

Affinity-purified proteins from BioID experiments and affinity-purified vesicles from anti-HA immunoisolation were buffered with 200 mM

HEPES (4-(2-hydroxyethyl)-1-piperazineethanesulfonic acid) pH 7.5. Disulfide bonds were reduced using 5 mM dithiothreitol (Sigma-Aldrich) at 37 °C for 1 h, followed by alkylation of cysteine residues using 15 mM iodoacetamide (Sigma-Aldrich) in the dark at RT for 1 h. Excessive iodoacetamide was quenched using 10 mM dithiothreitol. Protein mixtures were diluted in 1:6 ratio (v/v) using ultrapure water prior to digestion using sequencing grade trypsin (Worthington Biochemical) at 37 °C for 16 h. Digested peptides were subsequently desalted using self-packed C18 STAGE tips (3 M Empore™)⁵⁴ for LC-MS/MS analysis. Desalted peptides were resolubilized in 0.1% (v/v) formic acid and loaded onto HPLC-MS/MS system for analysis on an Orbitrap Q-Exactive Exploris 480 (Thermo Fisher Scientific) mass spectrometer coupled to an FAIMS Pro Interface system and Easy nanoLC 1000 (Thermo Fisher Scientific) with a flow rate of 300 nl/min. The stationary phase buffer was 0.1% formic acid, and mobile phase buffer was 0.1% (v/v) formic acid in 80% (v/v) acetonitrile. Chromatography for peptide separation was performed using increasing organic proportion of acetonitrile (5–40% (v/v) over a 120 min gradient) on a self-packed analytical column using PicoTip™ emitter (New Objective, Woburn, MA) using Reprosil Gold 120 C-18, 1.9 μm particle size resin (Dr. Maisch, Ammerbuch-Entringen, Germany). The mass spectrometry analyzer operated in data independent acquisition mode at a mass range of 300–2000 Da, compensation voltages of –50/–70 CVs with survey scan of 120,000 and 15,000 resolutions at MS1 and MS2 levels, respectively. Mass spectrometry data were processed by Spectronaut™ software version 15 (Biognosys AG)⁵⁵ using direct-DIATM analysis using default settings, including: oxidized methionine residues, biotinylation, protein N-terminal acetylation as variable modification, cysteine carbamidomethylation as fixed modification, initial mass tolerance of MS1 and MS2 of 15 ppm. Protease specificity was set to trypsin with up to 2 missed cleavages allowed. Only peptides longer than seven amino acids were analyzed, and the minimal ratio count to quantify a protein was 2 (proteome only). The false discovery rate (FDR) was set to 1% for peptide and protein identifications. Database searches were performed against the UniProt Chlorocebus sabaues (Green monkey) database containing 19,232 entries (December 2021). High precision iRT calibration was used for samples processed using the same nanospray conditions⁵⁶. Protein tables were filtered to eliminate identifications from the reverse database and also common contaminants. The SynGO enrichment tool⁴³ was used to analyze the proteins that enriched in synaptophysin-HA and ATG9A-HA samples.

Immunoisolation of synaptic vesicles

AP4E1 KO mice [strain #09451 (C57BL/6N-Ap4e1^{tm1b(KOMP)Wtsis})] from EMMA, Infrafrontier. Littermate wild type control and KO mouse whole brains (8-month-old) were homogenized in ice-cold KPBS buffer²⁶ (136 mM KCl, 10 mM KH₂PO₄, pH 7.25) supplemented with cComplete EDTA-free protease inhibitor. After 40 strokes, lysates were centrifuged at 17,000 × g for 5 min followed by a second round of centrifugation at 17,000 × g for 5 min to pellet unbroken cells and debris. The resulting supernatant was transferred to new tubes and the protein concentration was estimated with the Pierce BCA protein Assay kit (Thermo Scientific). To immunoisolate synaptic vesicles, VAMP2 antibodies were pre-incubated with Dynabeads™ Protein G (Thermo Scientific) in 200 μl PBS with 0.02% Tween-20 with rotation for 30 min at RT. VAMP2-conjugated Dynabeads™ magnetic beads were washed once with KPBS buffer and then added to the brain lysates with rotation at 4 °C. Following overnight incubation, the beads were washed three times and processed for immunoblot.

Statistics and reproducibility

Data are presented as mean ± SD or SEM, with n indicating the number of independent experiments. Statistical significance was

determined using the two-sided Student's *t*-test or two-sided paired *t*-test for the comparison of two independent groups. The one-way ANOVA followed by Tukey's honest significant difference (HSD) post hoc test was applied for multiple comparisons. Relevant *p*-values are presented in the figure legends. All representative light microscopy images and Western blot images were obtained from at least three independent experiments with similar results. CLEM experiments and in vitro assays were performed twice, and representative images are shown. Proximity biotinylation and immunoisolation of vesicles for proteomic analysis were repeated three times. All images were analyzed with ImageJ 1.53q and Sigma plot, Origin 2022b and Sigma plot (ver 10.0) were used for statistical comparisons.

Reporting summary

Further information on research design is available in the Nature Portfolio Reporting Summary linked to this article.

Data availability

Data supporting the findings of this study not shown in the figures are available in the Supplementary Information, Supplementary Movies and Source Data, and are also available from the corresponding author upon request. The mass spectrometry proteomics data have been deposited to the ProteomeXchange Consortium via the PRIDE⁵⁷ partner repository with the dataset identifier PXD037490. Source data are provided with this paper.

References

- De Camilli, P., Haucke, V., Takei, K. & Mugnaini, E. in *Synapses* (eds. Cowan, W. M., Südhof, T. C., Stevens, C. F.) 89–133 (The Johns Hopkins University Press, 2001).
- Katz, B. The Croonian Lecture—The transmission of impulses from nerve to muscle, and the subcellular unit of synaptic action. *Proc. R. Soc. Lond. Ser. B. Biol. Sci.* **155**, 455–477 (1962).
- Heuser, J. E. & Reese, T. S. Evidence for recycling of synaptic vesicle membrane during transmitter release at the frog neuromuscular junction. *J. Cell Biol.* **57**, 315–344 (1973).
- Ceccarelli, B., Hurlbut, W. P. & Mauro, A. Turnover of transmitter and synaptic vesicles at the frog neuromuscular junction. *J. Cell Biol.* **57**, 499–524 (1973).
- Saheki, Y. & De Camilli, P. Synaptic vesicle endocytosis. *Cold Spring Harb. Perspect. Biol.* **4**, a005645 (2012).
- Kononenko, N. L. & Haucke, V. Molecular mechanisms of presynaptic membrane retrieval and synaptic vesicle reformation. *Neuron* **85**, 484–496 (2015).
- Milovanovic, D. & De Camilli, P. Synaptic vesicle clusters at synapses: a distinct liquid phase? *Neuron* **93**, 995–1002 (2017).
- Pechstein, A. et al. Vesicle clustering in a living synapse depends on a synapsin region that mediates phase separation. *Cell Rep.* **30**, 2594–2602.e2593 (2020).
- Milovanovic, D., Wu, Y., Bian, X. & De Camilli, P. A liquid phase of synapsin and lipid vesicles. *Science* **361**, 604–607 (2018).
- De Camilli, P., Harris, S. M. Jr, Huttner, W. B. & Greengard, P. Synapsin I (Protein I), a nerve terminal-specific phosphoprotein. II. Its specific association with synaptic vesicles demonstrated by immunocytochemistry in agarose-embedded synaptosomes. *J. Cell Biol.* **96**, 1355–1373 (1983).
- Südhof, T. C. et al. Synapsins: mosaics of shared and individual domains in a family of synaptic vesicle phosphoproteins. *Science* **245**, 1474–1480 (1989).
- Gitler, D. et al. Different presynaptic roles of synapsins at excitatory and inhibitory synapses. *J. Neurosci.* **24**, 11368–11380 (2004).
- Pieribone, V. A. et al. Distinct pools of synaptic vesicles in neurotransmitter release. *Nature* **375**, 493–497 (1995).

14. Sopova, E. & Shupliakov, O. Two distinct mechanisms for synaptic vesicle clustering in vertebrate axons. *Eur. Neuropharmacol.* **29**, S264 (2019).
15. Park, D. et al. Cooperative function of synaptophysin and synapsin in the generation of synaptic vesicle-like clusters in non-neuronal cells. *Nat. Commun.* **12**, 263 (2021).
16. Cameron, P. L., Sudhof, T. C., Jahn, R. & De Camilli, P. Colocalization of synaptophysin with transferrin receptors: implications for synaptic vesicle biogenesis. *J. Cell Biol.* **115**, 151–164 (1991).
17. Johnston, P. A. et al. Synaptophysin is targeted to similar microvesicles in CHO and PC12 cells. *EMBO J.* **8**, 2863–2872 (1989).
18. Maeda, S. et al. Structure, lipid scrambling activity and role in autophagosome formation of ATG9A. *Nat. Struct. Mol. Biol.* **27**, 1194–1201 (2020).
19. Matoba, K. et al. Atg9 is a lipid scramblase that mediates autophagosomal membrane expansion. *Nat. Struct. Mol. Biol.* **27**, 1185–1193 (2020).
20. Ghanbarpour, A., Valverde, D. P., Melia, T. J. & Reinisch, K. M. A model for a partnership of lipid transfer proteins and scramblases in membrane expansion and organelle biogenesis. *Proc. Natl Acad. Sci. USA* **118**, e2101562118 (2021).
21. Claude-Taupin, A. et al. ATG9A protects the plasma membrane from programmed and incidental permeabilization. *Nat. Cell Biol.* **23**, 846–858 (2021).
22. Guardia, C. M. et al. Structure of human ATG9A, the only transmembrane protein of the core autophagy machinery. *Cell Rep.* **31**, 107837 (2020).
23. Yang, S. et al. Presynaptic autophagy is coupled to the synaptic vesicle cycle via ATG-9. *Neuron* **110**, 824–840 e810 (2022).
24. Yamaguchi, J. et al. Atg9a deficiency causes axon-specific lesions including neuronal circuit dysgenesis. *Autophagy* **14**, 764–777 (2018).
25. Xuan, Z. et al. The active zone protein Clarinet regulates ATG-9 trafficking at synapses and presynaptic autophagy. Preprint at *bioRxiv*, <https://doi.org/10.1101/2021.08.19.457026> (2021).
26. Chantranupong, L. et al. Rapid purification and metabolomic profiling of synaptic vesicles from mammalian brain. *Elife* **9**, e59699 (2020).
27. Taoufiq, Z. et al. Hidden proteome of synaptic vesicles in the mammalian brain. *Proc. Natl Acad. Sci. USA* **117**, 33586–33596 (2020).
28. Bradberry, M. M. et al. Rapid and gentle immunopurification of brain synaptic vesicles. *J. Neurosci.* **42**, 3512–3522 (2022).
29. Takamori, S. et al. Molecular anatomy of a trafficking organelle. *Cell* **127**, 831–846 (2006).
30. Giordano, F. et al. PI(4,5)P(2)-dependent and Ca(2+)-regulated ER-PM interactions mediated by the extended synaptotagmins. *Cell* **153**, 1494–1509 (2013).
31. Fletcher, T. L., Cameron, P., De Camilli, P. & Banker, G. The distribution of synapsin I and synaptophysin in hippocampal neurons developing in culture. *J. Neurosci.* **11**, 1617–1626 (1991).
32. Kato, M. & McKnight, S. L. A solid-state conceptualization of information transfer from gene to message to protein. *Annu. Rev. Biochem.* **87**, 351–390 (2018).
33. Lin, Y. et al. Toxic PR poly-dipeptides encoded by the C9orf72 repeat expansion target LC domain polymers. *Cell* **167**, 789–802 e712 (2016).
34. Mattera, R., Park, S. Y., De Pace, R., Guardia, C. M. & Bonifacino, J. S. AP-4 mediates export of ATG9A from the trans-golgi network to promote autophagosome formation. *Proc. Natl Acad. Sci. USA* **114**, E10697–E10706 (2017).
35. Kannagara, A. R. et al. Biold reveals an ATG9A interaction with ATG13-ATG101 in the degradation of p62/SQSTM1-ubiquitin clusters. *EMBO Rep.* **22**, e51136 (2021).
36. Branon, T. C. et al. Efficient proximity labeling in living cells and organisms with TurboID. *Nat. Biotechnol.* **36**, 880–887 (2018).
37. Davies, A. K. et al. AP-4 vesicles contribute to spatial control of autophagy via RUSC-dependent peripheral delivery of ATG9A. *Nat. Commun.* **9**, 3958 (2018).
38. Guardia, C. M. et al. RUSC2 and WDR47 oppositely regulate kinesin-1-dependent distribution of ATG9A to the cell periphery. *Mol. Biol. Cell* **32**, ar25 (2021).
39. Rivero-Rios, P. & Weisman, L. S. Roles of PIKfyve in multiple cellular pathways. *Curr. Opin. Cell Biol.* **76**, 102086 (2022).
40. Lin, M. G. & Hurlley, J. H. Structure and function of the ULK1 complex in autophagy. *Curr. Opin. Cell Biol.* **39**, 61–68 (2016).
41. Slepnev, V. I., Ochoa, G. C., Butler, M. H. & De Camilli, P. Tandem arrangement of the clathrin and AP-2 binding domains in amphiphysin 1 and disruption of clathrin coat function by amphiphysin fragments comprising these sites. *J. Biol. Chem.* **275**, 17583–17589 (2000).
42. Nemoto, Y. et al. Identification and characterization of a synaptotagmin 2 splice isoform predominantly expressed in nerve terminals. *J. Biol. Chem.* **276**, 41133–41142 (2001).
43. Koopmans, F. et al. SynGO: an evidence-based, expert-curated knowledge base for the synapse. *Neuron* **103**, 217–234.e214 (2019).
44. De Pace, R. et al. Altered distribution of ATG9A and accumulation of axonal aggregates in neurons from a mouse model of AP-4 deficiency syndrome. *PLoS Genet.* **14**, e1007363 (2018).
45. Ivankovic, D. et al. Axonal autophagosome maturation defect through failure of ATG9A sorting underpins pathology in AP-4 deficiency syndrome. *Autophagy* **16**, 391–407 (2020).
46. Majumder, P. et al. AP-4 regulates neuronal lysosome composition, function, and transport via regulating export of critical lysosome receptor proteins at the trans-Golgi network. *Mol. Biol. Cell* **33**, ar102 (2022).
47. Emperador-Melero, J. & Kaeser, P. S. Assembly of the presynaptic active zone. *Curr. Opin. Neurobiol.* **63**, 95–103 (2020).
48. Wu, X. et al. RIM and RIM-BP form presynaptic active-zone-like condensates via phase separation. *Mol. Cell* **73**, 971–984 e975 (2019).
49. Emperador-Melero, J. et al. PKC-phosphorylation of Liprin-alpha3 triggers phase separation and controls presynaptic active zone structure. *Nat. Commun.* **12**, 3057 (2021).
50. McDonald, N. A., Fetter, R. D. & Shen, K. Assembly of synaptic active zones requires phase separation of scaffold molecules. *Nature* **588**, 454–458 (2020).
51. Chen, X., Wu, X., Wu, H. & Zhang, M. Phase separation at the synapse. *Nat. Neurosci.* **23**, 301–310 (2020).
52. Park, D. et al. Impairment of release site clearance within the active zone by reduced SCAMP5 expression causes short-term depression of synaptic release. *Cell Rep.* **22**, 3339–3350 (2018).
53. Cao, M., Park, D., Wu, Y. & De Camilli, P. Absence of Sac2/INPP5F enhances the phenotype of a Parkinson’s disease mutation of synaptotagmin 1. *Proc. Natl Acad. Sci. USA* **117**, 12428–12434 (2020).
54. Rappsilber, J., Ishihama, Y. & Mann, M. Stop and go extraction tips for matrix-assisted laser desorption/ionization, nano electrospray, and LC/MS sample pretreatment in proteomics. *Anal. Chem.* **75**, 663–670 (2003).
55. Bruderer, R. et al. Extending the limits of quantitative proteome profiling with data-independent acquisition and application to acetaminophen-treated three-dimensional liver microtissues. *Mol. Cell Proteom.* **14**, 1400–1410 (2015).
56. Bruderer, R., Bernhardt, O. M., Gandhi, T. & Reiter, L. High-precision iRT prediction in the targeted analysis of data-independent acquisition and its impact on identification and quantitation. *Proteomics* **16**, 2246–2256 (2016).

57. Perez-Riverol, Y. et al. The PRIDE database resources in 2022: a hub for mass spectrometry-based proteomics evidences. *Nucleic Acids Res.* **50**, D543–D552 (2022).

Acknowledgements

We thank members of the De Camilli lab for discussion, Frank Wilson and Alina Vulpe for technical assistance. We thank Drs. Wade Harper, Miguel Gonzalez-Lozano, Tobias Walther and Zon Weng Lai (all from Harvard) for help and discussion with LC-MS/MS experiments. This research was supported in part by grants from the NIH (NS36251 and DA018343) and the Parkinson Foundation (PF-RCE-1946) to P.D.C. and a fellowship from the National Research Foundation of Korea (2019R1A6A3A03031300) to D.P.

Author contributions

D.P. and P.D.C. designed the experiments. Y. W., X.W., and A. B. performed CLEM experiments, protein purification/cell-free assays and LC-MS/MS, respectively, in collaboration with D.P. and S.G. collaborated in experiments involving AP4E1 KO mice. D.P. performed everything else. D.P. and P.D.C. wrote the paper. All authors read and approved the final manuscript.

Competing interests

P.D.C. is a member of the Scientific Advisory Board of Casma Therapeutics but declares no competing interest with this study. The other authors have no competing interests.

Additional information

Supplementary information The online version contains supplementary material available at <https://doi.org/10.1038/s41467-023-36081-3>.

Correspondence and requests for materials should be addressed to Pietro De Camilli.

Peer review information *Nature Communications* thanks Volker Haucke, Oleg Shupliakov and the anonymous reviewers for their contribution to the peer review of this work.

Reprints and permissions information is available at <http://www.nature.com/reprints>

Publisher's note Springer Nature remains neutral with regard to jurisdictional claims in published maps and institutional affiliations.

Open Access This article is licensed under a Creative Commons Attribution 4.0 International License, which permits use, sharing, adaptation, distribution and reproduction in any medium or format, as long as you give appropriate credit to the original author(s) and the source, provide a link to the Creative Commons license, and indicate if changes were made. The images or other third party material in this article are included in the article's Creative Commons license, unless indicated otherwise in a credit line to the material. If material is not included in the article's Creative Commons license and your intended use is not permitted by statutory regulation or exceeds the permitted use, you will need to obtain permission directly from the copyright holder. To view a copy of this license, visit <http://creativecommons.org/licenses/by/4.0/>.

© The Author(s) 2023